


Integrable turbulence and statistical characteristics of chaotic wave field in the Kundu-Eckhaus equation

Min Li^{1,*}, Xiao-Zhang Zhu¹ and Tao Xu^{2,3,†}

¹*School of Mathematics and Physics, North China Electric Power University, Beijing 102206, People's Republic of China*

²*State Key Laboratory of Heavy Oil Processing, China University of Petroleum, Beijing 102249, People's Republic of China*

³*Department of Mathematics, College of Science, China University of Petroleum, Beijing 102249, People's Republic of China*

 (Received 23 August 2023; revised 31 October 2023; accepted 27 November 2023; published 4 January 2024)

Integrable turbulence, as an irregular behavior in dynamic systems, has attracted a lot of attention in integrable and Hamiltonian systems. This article focuses on the studies of integrable turbulence phenomena of the Kundu-Eckhaus (KE) equation as well as the generation of rogue waves from the numerical and statistical viewpoints. First, via the Fourier collocation method, we obtain the spectral portraits of different analytical solutions. Second, we perform the numerical simulation on the KE equation under the initial condition of a plane wave with random noise to simulate the chaotic wave fields. Then, we analyze the influences of standard deviation and correlation length on the integrable turbulence and amplitude of wave field. It's found that both of the two parameters have positive effects on the generation probability of rogue wave caused by the interactions. But only the variation of standard deviation can lead to the transition from the breather turbulence to soliton turbulence. Furthermore, by analyzing the effects of additional higher-order nonlinear terms on the chaotic wave field, we find that those two higher-order nonlinear effects in the KE equation can lead to a larger amplitude of the chaotic wave field and a higher probability of generating rogue waves compared with the NLS equation.

DOI: [10.1103/PhysRevE.109.014204](https://doi.org/10.1103/PhysRevE.109.014204)

I. INTRODUCTION

Integrable turbulence is the irregular behavior of a dynamic system characterized by chaotic changes in flow parameters and can be defined by the relative number of solitons and breathers in the chaotic field. In the two extreme cases, it can be divided into soliton dominated turbulence and breather dominated turbulence [1]. The chaotic wave fields can be stimulated by the modulation instability or initial condition with high amplitude chaotic components. Recently, the generation of rogue waves in chaotic wave fields has always been a hot research direction. Rogue wave, as a research hotspot in nonlinear science, was first used by oceanographers to describe sudden and peculiar large amplitude waves in the ocean [2–4]. It usually has the following main characteristics: high peaks and deep valleys, and the time from emergence to disappearance is very short. Later, rogue waves were also observed in the fields of nonlinear optical fiber, super fluid mechanics, and plasma physics [5–12].

As we know, modulation instability (MI) plays an important role in the generation of rogue waves [13–15]. In particular, the noise-derived MI in the integrable system may evolve into a stable chaotic wave field where the integrable turbulence can arise [16–18]. Reference [16] used the numerical methods to study the turbulence phenomenon in the nonlinear Schrödinger (NLS) equation, and discussed the probability of generating rogue waves in chaotic fields.

Further, experiments in Ref. [19] showed the early stages of integrable turbulence in unidirectional deep water gravity waves and the appearance of Peregrine solitons in the integrable turbulence of unidirectional deep water gravity waves. Reference [18] studied the spectral characteristics of spatial Lax pair with different potentials and the generation mechanism of rogue waves under different driven conditions for the integrable Hirota equation. Besides, the properties of integrable turbulence and the formation of rogue waves in a coupled NLS system and fifth-order NLS equation have been investigated in Refs. [17,20].

In this paper, we focus on the Kundu-Eckhaus (KE) equation as follows:

$$iu_t + u_{xx} + 2|u|^2u + 4\beta^2|u|^4u - 4i\beta(|u|^2)_xu = 0, \beta \in R, \quad (1)$$

which is an integrable extension of the NLS equation in addition to the quintic term with a derivative term. Here u is a complex function of x and t which denotes the electromagnetic wave, β^2 is a real quintic nonlinearity coefficient, the fourth-term represents non-Kerr nonlinear effect, and the last term is a nonlinear self-frequency shift effect generated by the time-retarded induced Raman process. Equation (1) can be used to describe the propagation of ultrashort femtosecond pulses in an optical fiber. Moreover, such equation also has applications in quantum field theory [21], weakly nonlinear dispersive matter waves [22], and nonlinear optics [23]. The integrability of Eq. (1) has been intensively studied in the form of Lax pair, Painlevé property and Hamiltonian structure [24–28]. Furthermore, soliton, breather, and higher-order

*Corresponding author: ml85@ncepu.edu.cn

†Corresponding author: xutao@cup.edu.cn

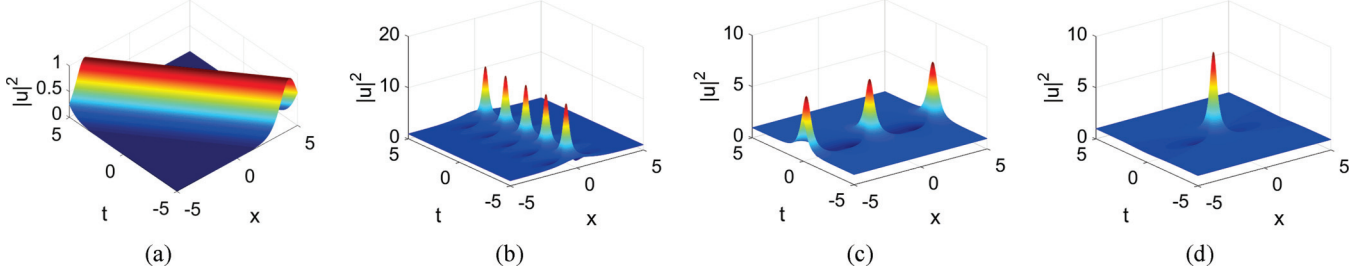


FIG. 1. Analytical solutions of Eq. (1) with $\beta = 0.01$: (a) The bright soliton with $\xi = 0.2$, $\eta = 0.5$, $\delta = 0$, $v_1 = 0.6$, and $\rho_1 = 0.4$ in Solution (3); (b) The temporally periodic breather solution with $\xi = 0$, $c = 1$, and $\eta = 1.2$ in Solution (4); (c) The spatially periodic breather solution with $\xi = 0$, $c = 1$, and $\eta = 0.75$ in Solution (4); (d) The rogue wave solution with $\xi = 0$, and $\eta = 1$ in Solution (5).

rogue wave solutions have also been given via the Darboux transformation and bilinear method [29–33].

Although the analytical solutions of Eq. (1) have been obtained, the spectral portraits of spatial Lax pair with those potentials have not been solved, which can be used to further analyze the integrable turbulence in the chaotic wave fields. Moreover, the soliton and breather turbulence, as well as rogue waves caused by the noise-derived modulational instabilities of Eq. (1), have not been revealed until now. Therefore, in Sec. II, we solve the eigenvalue problem of Lax pair numerically and give the spectral characteristics corresponding different analytical solutions of Eq. (1). Then, in Sec. III, we

use a plane wave with random noise as the initial condition to simulate the chaotic wave fields numerically. Furthermore, we analyze the effects of different parameters on the statistical quantities of chaotic wave fields and generation probability of rogue waves. Finally, we address the conclusions and discussions of this paper in Sec. IV.

II. SPECTRAL PORTRAITS OF ANALYTICAL SOLUTIONS FOR THE KE EQUATION

As KE equation is integrable, the Lax pair of Eq. (1) has been given as [29]

$$\psi_x = U\psi, \quad \psi_t = (V_2\lambda^2 + V_1\lambda + V_0)\psi, \quad (2a)$$

$$U = \begin{pmatrix} -i\lambda + i\beta|u|^2 & u \\ -u^* & i\lambda - i\beta|u|^2 \end{pmatrix}, \quad V_2 = \begin{pmatrix} -2i & 0 \\ 0 & 2i \end{pmatrix}, \quad V_1 = \begin{pmatrix} 0 & 2u \\ -2u^* & 0 \end{pmatrix}, \quad (2b)$$

$$V_0 = \begin{pmatrix} \beta(-u_x u^* + uu_x^*) + 4i\beta^2|u|^4 + i|u|^2 & iu_x + 2\beta|u|^2 u \\ iu_x^* - 2\beta|u|^2 u^* & -\beta(-u_x u^* + uu_x^*) - 4i\beta^2|u|^4 - i|u|^2 \end{pmatrix}, \quad (2c)$$

where $\psi = (\psi_1, \psi_2)^T$ (T represents the transposition of a vector) is the vector eigenfunction, ψ_1 and ψ_2 are scalar eigenfunctions related to x and t , λ is the spectral parameter, and $u(x, t)$ is the potential function. The compatibility condition $\psi_{xt} = \psi_{tx}$ can lead to Eq. (1).

The results of the inverse scattering technique [34] indicate that the spectra of the eigenvalues of Eq. (2) does not depend on the time t . Therefore, the dynamics of the field $u(x, t)$ at any time t could be analyzed by the spectra of the eigenvalues of Eq. (2) at the initial condition $u(x, 0)$. For different initial potential functions, the set of eigenvalues λ and eigenfunctions ψ are different. In the following, we will analyze the correspondence between the analytical solutions and spectral portraits. The analytical soliton, spatially and temporally periodic breather, and rogue wave solutions of Eq. (2) have been obtained and listed respectively as follows (here we assume $\lambda = \xi + i\eta$).

(1) The fundamental bright soliton [33]:

$$u = -2\eta \exp[i f(x, t)] \operatorname{sech}(2\eta x + 8\xi\eta t - \delta), \quad (3a)$$

$$f(x, t) = -2\xi x - 4(\xi^2 - \eta^2)t - v_1 + 2\rho_1 + 4\beta\eta \exp(2\eta x + 8\xi\eta t - \delta) \times \operatorname{sech}(2\eta x + 8\xi\eta t - \delta), \quad (3b)$$

where δ , v_1 , and ρ_1 are real constants. By choosing the parameters $\beta = 0.01$, $\xi = 0.2$, $\eta = 0.5$, $\delta = 0$, $v_1 = 0.6$, and $\rho_1 = 0.4$, the propagation of single bright soliton is shown in Fig. 1(a). The real part of the eigenvalue is related to velocity of soliton, while the imaginary part affects the amplitude of soliton.

(2) The single breather [30]:

$$u = \frac{b_{11}}{b_{12}} \exp\left(i\left(\rho + \frac{b_{13}}{b_{12}}\right)\right), \quad (4a)$$

$$\rho = ax + bt, \quad a = -2\xi + 2\beta c^2, \quad b = -a^2 + 4\beta^2 c^4 + 2c^2, \quad (4b)$$

$$b_{11} = -c\eta \cos(\theta_1) - c^2 \cosh(\theta_2) - 2i\eta K_0 \sinh(\theta_2) + 2\eta^2 \cosh(\theta_2), \quad (4c)$$

$$b_{12} = \eta \cos(\theta_1) - c \cosh(\theta_2), \quad b_{13} = -4\beta\eta K_0 \sin(\theta_1), \quad (4d)$$

$$\theta_1 = 2K_0(x + 4\xi t), \quad \theta_2 = 4tK_0\eta, \quad K_0 = \sqrt{c^2 - \eta^2}, \quad (4e)$$

where a , b , and c are all real constants. If $K_0^2 < 0$ and $\xi = 0$, a temporally periodic breather can be obtained by choosing

$c = 1$ and $\eta = 1.2$ as shown in Fig. 1(b). If $K_0^2 > 0$ and $\xi = 0$, a spatially periodic breather is derived by choosing $c = 1$ and $\eta = 0.75$, as shown in Fig. 1(c).

(3) The fundamental rogue wave [30]:

$$u = \frac{L_1}{L_2} \exp\left(i\left(\rho + \frac{L_3}{L_2}\right)\right), \quad (5a)$$

$$L_1 = (-64\eta^2\xi^2t^2 - 16\eta^4t^2 - 32\eta^2\xi tx - 4\eta^2x^2 + 16i\eta^2t + 3)\eta, \quad (5b)$$

$$L_2 = 16\eta^4t^2 + 64\eta^2\xi^2t^2 + 32\eta^2\xi tx + 4\eta^2x^2 + 1, \quad (5c)$$

$$L_3 = 16\beta\eta^2x + 64\beta\eta^2t\xi, \quad (5c)$$

which can be obtained from the limit $c \rightarrow \eta$ in Solution (4). By setting $\xi = 0$, and $\eta = 1$, the evolution of rogue waves can be seen in Fig. 1(d).

To solve Lax pair (2) with the above solutions as the initial potential function, we rewrite the spatial part as a standard linear eigenvalue problem:

$$\begin{pmatrix} i\beta|u|^2 - \frac{\partial}{\partial x} & u \\ u^* & i\beta|u|^2 + \frac{\partial}{\partial x} \end{pmatrix} \begin{pmatrix} \psi_1 \\ \psi_2 \end{pmatrix} = i\lambda \begin{pmatrix} \psi_1 \\ \psi_2 \end{pmatrix}. \quad (6)$$

For general potential function $u(x, t)$, it is difficult to find the spectra analytically. In this article, we apply the Fourier collocation method [35] to solve Eq. (6) numerically. First, we truncate the x axis into a finite interval of length L , and expand $\psi_1(x)$, $\psi_2(x)$, and $u(x, t)$ into the Fourier series:

$$\psi_1 = \sum_{n=-N}^N a_{1n} e^{ink_0x}, \quad \psi_2 = \sum_{n=-N}^N a_{2n} e^{ink_0x}, \quad (7)$$

$$u = \sum_{n=-N}^N b_n e^{ink_0x}, \quad u^* = \sum_{n=-N}^N b_n^* e^{-ink_0x},$$

$$uu^* = \sum_{n=-N}^N c_n e^{ink_0x}, \quad (8)$$

where $k_0 = \frac{2\pi}{L}$ and $t = t_0$ are given. By substituting Eqs. (7) and (8) into Eq. (6), and equating the coefficients of the same Fourier mode, we can obtain the spectra portraits. Figures 2(a1)–2(a4) describe the profiles of four exact solutions in Fig. 1 at $t = 0$, $t = 0.1$, and $t = 0.2$. Figures 2(b1) and 2(b2) are their corresponding spectra portraits about real and imaginary parts of eigenvalues [marked as $\text{Re}(\lambda)$ and $\text{Im}(\lambda)$, respectively], which indicate that the eigenvalues are independent of time. In details, it's found that there is a pair of complex conjugate points at $0.2 \pm 0.5i$ in Fig. 2(b1), which is consistent with the choice of $\lambda = 0.2 + 0.5i$ in Fig. 2(a1). Similarly, the temporally periodic breather solution in Fig. 2(a2) corresponds to a pair of complex conjugate points at $\pm 1.2i$ in Fig. 2(b2), the spectra of spatially periodic breather solution in Fig. 2(a3) is a pair of complex conjugate points at $\pm 0.75i$ in Fig. 2(b3), and the rogue wave solution in Fig. 2(a4) corresponds to a pair of complex conjugate points at $\pm i$ in Fig. 2(b4).

III. NUMERICAL SIMULATION OF CHAOTIC WAVE FIELDS IN EQ. (1)

In this section, we use the split-step Fourier (SSF) method to perform numerical simulations on Eq. (1) under the initial

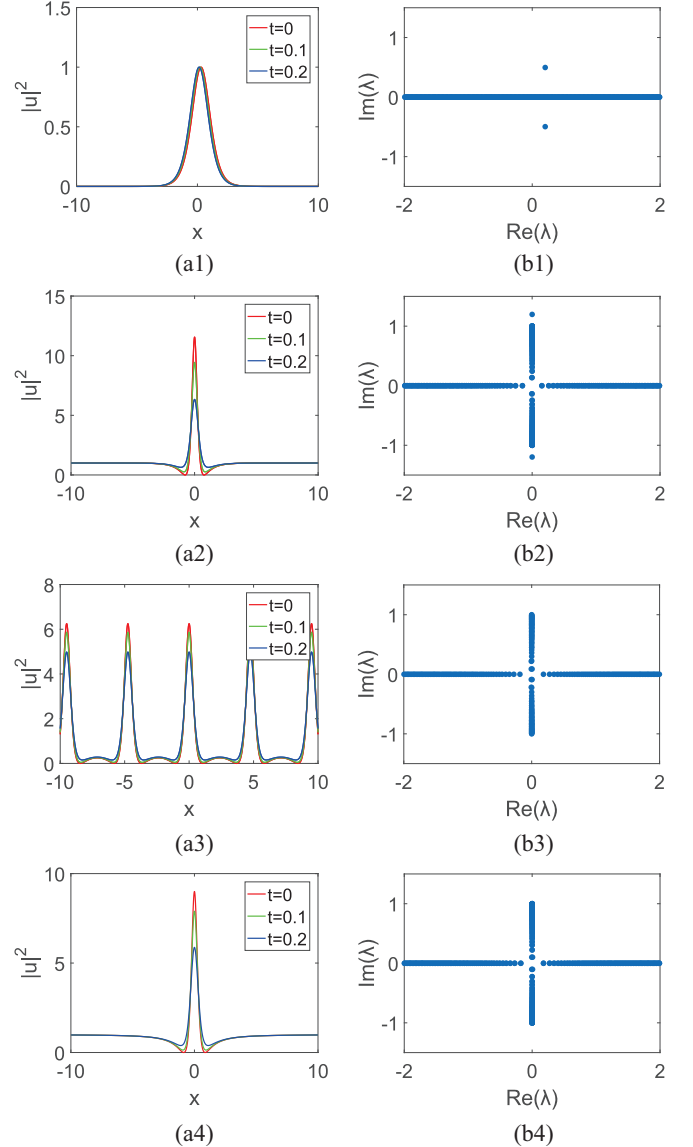


FIG. 2. (a1)–(a4) Profiles of $|u|^2$ in Figs. 1(b1)–1(b4); The corresponding spectra portraits of Figs. 2(a1)–2(a4).

condition of a plane wave with random noise. We will study the statistical properties of soliton and breather turbulence in the chaotic wave fields and then analyze the generation of rogue wave caused by the soliton and breather interactions in integrable turbulence. In the following, due to the sensitivity of numerical simulation to the coefficient β of the fifth-order nonlinear term, we set $\beta = 0.01$ in this section.

A. Split-step Fourier method

The basic idea of the SSF method is to divide the original problem into linear and nonlinear subproblems [36]. For Eq. (1), the linear part is

$$u_t = iu_{xx}, \quad (9)$$

and the nonlinear part is

$$u_t = 2i|u|^2u + 4i\beta^2|u|^4u + 4\beta(|u|^2)_xu. \quad (10)$$

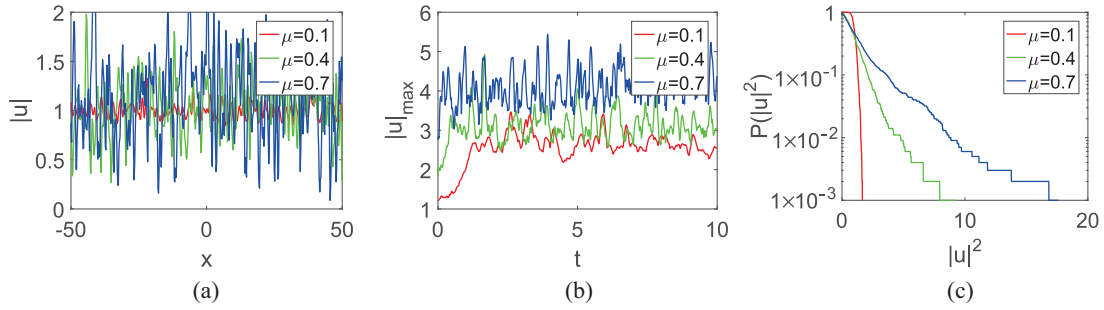


FIG. 3. Numerical results of initial conditions at three values of $\mu = 0.1$ (the red line), $\mu = 0.4$ (the green line), $\mu = 0.7$ (the blue line), with fixed value of $L_c = 0.5$. (a) Initial field intensity of $u(0, x)$; (b) Evolution of the maximum field amplitude versus t ; (c) Probability density function for the field intensity after 100 units along the t axis.

The spatial grid points are given by $X_j = 2\pi j/N$, $j = 0, 1, 2, \dots, N$ and the approximate solution to $u(X_j, t)$ is denoted by $U_j(t)$. First, we use a discrete Fourier transform to solve the linear part and obtain the iteration in time:

$$U_j^{m+1} = F_j^{-1}[F(U_j^m)\exp(-ik^2\Delta t)], \quad (11)$$

where F and F^{-1} represents respectively the Fourier transform and inverse Fourier transform, Δt is time step, and U_j^m denotes the approximation to $u(X_j, m\Delta t)$. Then the spatial discretization of the nonlinear part can be written as

$$\dot{U}_j = 2i|U_j|^2U_j + 4i\beta^2|U_j|^4U_j + 4\beta F^{-1}(ikF(|U_j|^2))U_j, \quad (12)$$

where the superimposed point represents the differentiation over time, and for the time integration of Eq. (12), we use the fourth-order Runge-Kutta method which exhibits superior conservation of energy and other invariants [37].

B. Chaotic wave fields generated by unstable modulation driven by a plane wave with random noise

To simulate the chaotic wave fields, we use a plane wave with random noise as the initial condition,

$$u(x, 0) = 1 + \mu f(x), \quad (13)$$

where $f(x)$ is a normalized complex random function with the standard deviation $\sigma = 1$, and μ gives the standard deviation of the entire function $u(x, 0)$ [6,16,38]. The numerical discretization of the real and imaginary part of $f(x)$ are both in the form of Gaussian distribution with $\sqrt{2\Delta x}/(\sqrt{\pi}L_c)\exp[-2(x_k/L_c)^2]$, where L_c is the variable correlation length. Since the initial condition is controlled by μ and L_c , we will study effects of those two parameters on the integrable turbulence phenomenon of Eq. (1).

Figure 3(a) shows the intensity distribution of $u(0, x)$ under three initial conditions with fixed correlation length L_c and different μ values. It can be clearly seen that the random deviation from the continuous wave with amplitude one is relatively small for the case of $\mu = 0.1$. While for the cases of $\mu = 0.4$ and $\mu = 0.7$, the chaotic deviation around the continuous wave significantly increases. This indicates that when the correlation length L_c is fixed, the chaotic bias of the initial condition $u(0, x)$ increases with the increase of μ

value. As we know, the initial random condition can drive the modulation instability to evolve the chaotic wave field [16,17]. We compute the maximum amplitude of the simulated chaotic wave field under the above initial conditions, which can be seen in Fig. 3(b). As expected by the modulation instability theory, for $\mu = 0.1$, the maximum amplitude value increases exponential growth at the initial stage of evolution. After propagating a distance, it converges to a chaotic state. The evolutions for the cases of $\mu = 0.4$ and $\mu = 0.7$ are similar, except that the convergence speeds to the chaotic state are faster and the peak amplitudes of the wave field are higher after reaching the chaotic state. This indicates that the greater the strength of the initial conditions, the shorter the time for the chaotic wave fields to converge to the chaotic state, and the higher the peak amplitude of the chaotic state. Besides, we compute the probability density function (PDF) because it is closely related to the probability of rogue waves appearing in chaotic wave fields [1,39]. Figure 3(c) shows the PDF of the field intensity obtained after propagating 100 units of distance along the t axis. It is clear that the larger the initial μ , the higher the corresponding PDF tail. Therefore, it can be predicted that the probability of generating rogue waves will significantly increase with the increase of μ value when the wave fields converge to a chaotic state.

The spectra portraits obtained by the Fourier collocation method under the initial condition (13) with different μ values are shown in Figs. 4(a1)–4(c1). When $\mu = 0.1$, it can be seen from Fig. 4(a1) that almost all the eigenvalues remain on the coordinate axis. While as the μ value increases, the eigenvalues begin to be scattered from the coordinate axis. This is because the real part of the eigenvalue $\lambda = \xi + i\eta$ is related to velocity, and the imaginary part is related to amplitude. The random noise in the chaotic fields leads to the generation of solitons with nonzero velocities. The corresponding eigenvalues possess both nonzero real and imaginary parts, resulting in the dispersion of eigenvalues from the coordinate axis and the increase in the number of solitons in the chaotic field. When the spectrum remains unchanged during propagation, the evolution of the chaotic wave field is defined by the relative number of solitons and breathers [16]. By using the SSF method for numerical simulation, we obtain the evolution of chaotic wave fields in Figs. 4(a2)–4(c2). It can be seen that the temporally and spatially periodic breathers are stimulated, which interact with each other in wave field [see

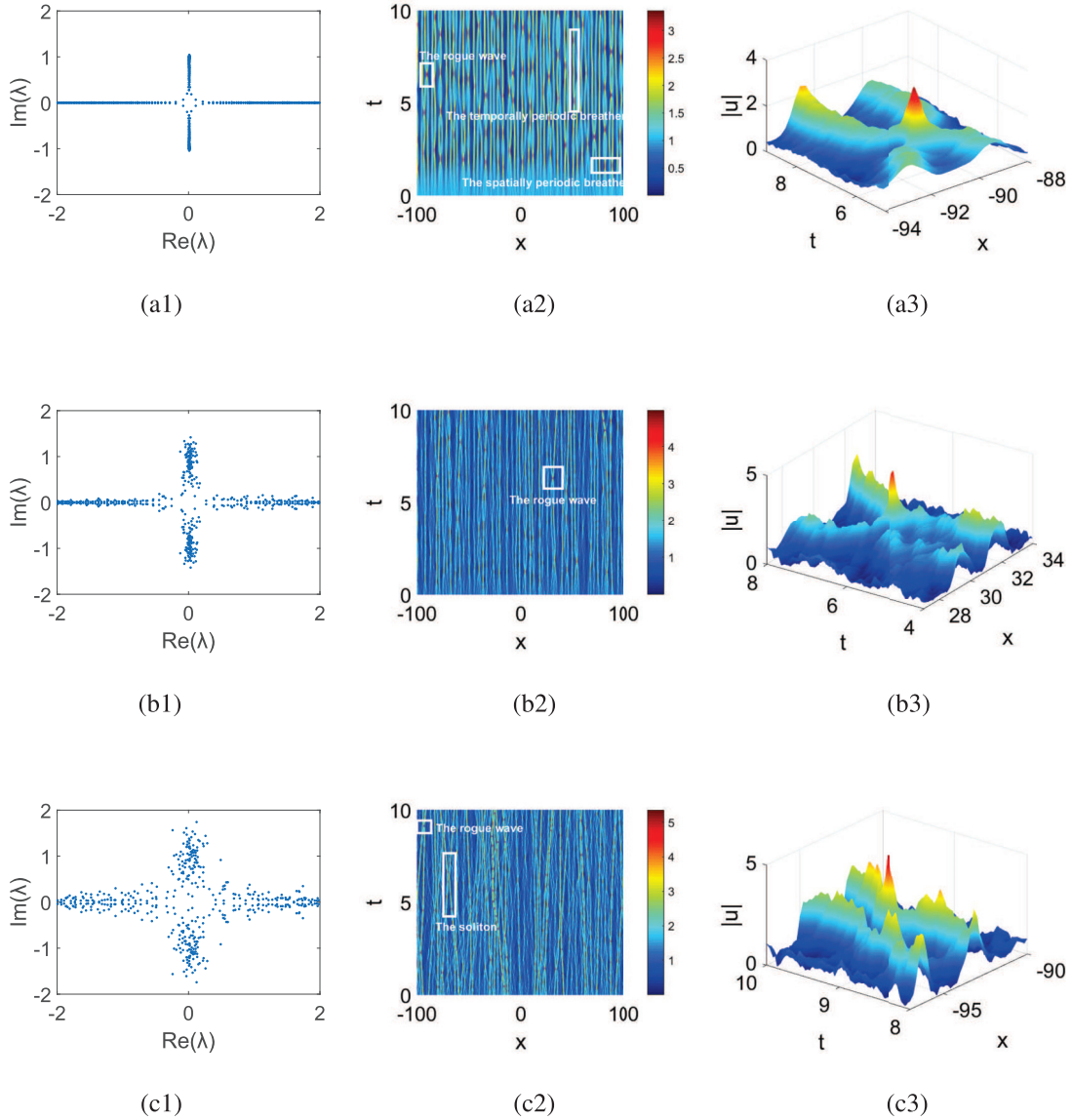


FIG. 4. Numerical results of initial conditions with fixed value of $L_c = 0.5$, and three different values of $\mu = 0.1$ (a1), (b1), (c1); $\mu = 0.4$ (a2), (b2), (c2); $\mu = 0.7$ (a3), (b3), (c3). [(a1)–(c1)] Spectra portraits; [(a2)–(c2)] Space-time diagrams of chaotic wave fields; [(a3)–(c3)] The three-dimensional view of the large amplitude structures extracted from [(a2)–(c2)].

Fig. 4(a2)]. When $\mu = 0.4$, the pattern is an intermediate state as shown in Fig. 4(b2), which corresponds to the interactions of breathers, solitons, as well as the background radiation waves. In Fig. 4(c2), the chaotic wave field is dominated by solitons. Figure 4 indicates that the chaotic field transforms from breather turbulence to soliton turbulence, which is consistent with the analysis on the spectra portraits. Furthermore, the amplitude value of the wave field is displayed on the right side of Figs. 4(a2)–4(c2). The peak amplitudes of the wave field are respectively 3.5, 4.5, and 5.5 for $\mu = 0.1$, $\mu = 0.4$, and $\mu = 0.7$. This indicates that as the μ value increases, the peak amplitude increases, and the possibility of rogue waves also increases. Figures 4(a3)–4(c3) are respectively the collisions among multiple breathers, breathers and solitons, and multiple solitons on the background radiation wave extracted from Figs. 4(a2)–4(c2). The large amplitude waves

generated by these three collisions are in fact the rogue waves because the peak values are about 3.2, 4.5, and 5, all of which are more than twice that of the background waves.

After the above analysis, we find that the chaotic wave field transitions from breather turbulence to soliton turbulence as the μ value increases. According to the results in Sec. II, the eigenvalues λ with both nonzero real and imaginary parts correspond to the solitons with nonzero velocities, the eigenvalues above i on the imaginary axis correspond to the temporally periodic breathers, the eigenvalues below i on the imaginary axis correspond to the spatially periodic breathers, and those points around the real axis correspond to the radiation waves. To further explain the process of transition from the statistic view, we calculate the proportion of eigenvalues corresponding to different kinds of solutions in the chaotic wave field and analyze the variation of solutions

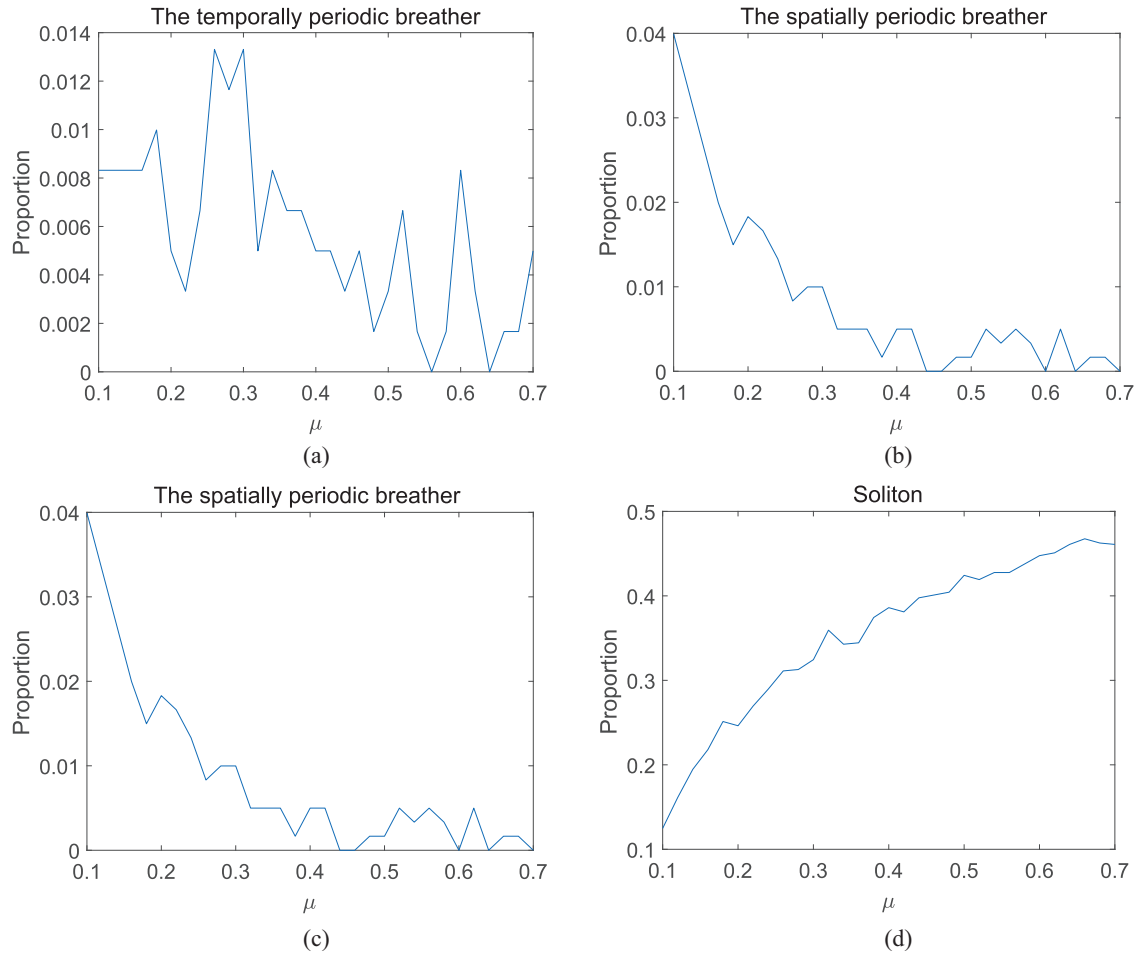


FIG. 5. Changes of wave content in the chaotic wave field with parameter μ . (a) The proportion of the temporally periodic breather. (b) The proportion of the spatially periodic breather. (c) The proportion of the radiation wave. (d) The proportion of soliton.

contents with μ values, as seen in Fig. 5. We find that the content of the temporally periodic breathers in the chaotic field is relatively small compared with other solutions, its proportion does not exceed 0.01, and an increase in μ value has little effect on it. Besides, the content of the spatially periodic breathers and radiation waves decrease, while the content of soliton solutions increases.

In the following, we will analyze the effect of the correlation length L_c on the evolution of chaotic wave fields, which is related to the oscillation frequency of initial condition. As shown in Fig. 6(a1), as the correlation length L_c increases the oscillation frequency decreases, but the amplitude is almost not affected. In Fig. 6(a2), the large value of L_c leads to the short convergence time to chaotic state, and the high peak amplitude of the wave field. Figure 6(a3) shows the PDF of the field intensity obtained after propagating 100 units of distance along the t axis. Similar to the case in Fig. 3(a3), the larger the value L_c , the higher the tail of the corresponding PDF. Therefore, it can be predicted that when the wave field converges to a chaotic state, the probability of generating rogue waves in chaotic wave fields with larger L_c values will significantly increase.

We also calculate the spectra of chaotic wave fields at different L_c values, which are shown in Figs. 7(a1)–7(c1). Different from the case of μ , the eigenvalues are all scattered around the coordinate axis for the three choices of L_c , which means the correlation length has little effect on the types of solutions in chaotic wave fields. But as the L_c value increases, the interval of imaginary parts of eigenvalues gradually increases, indicating that the amplitude of solitons in the chaotic wave fields increases. The evolution of the chaotic wave fields obtained through the SSF method in Figs. 7(a2)–7(c1) also shows the generation of breathers, solitons, as well as large amplitude waves and background radiation waves. Similar to the effects of parameter μ , the peak amplitude of wave field increases as L_c increases, which is consistent with the results of the PDF diagram in Fig. 6(a2). Figures 7(a3)–7(c3) show some high amplitude waves intercepted from Figs. 7(a2)–7(c2). Specifically, the peak amplitudes near the interacting points are around 4, 4.5, and 5.5, which are more than twice the amplitude of the background waves and can also be considered as rogue waves.

Since Eq. (1) can be transformed into the classical NLS equation when $\beta = 0$, we will demonstrate the influence of

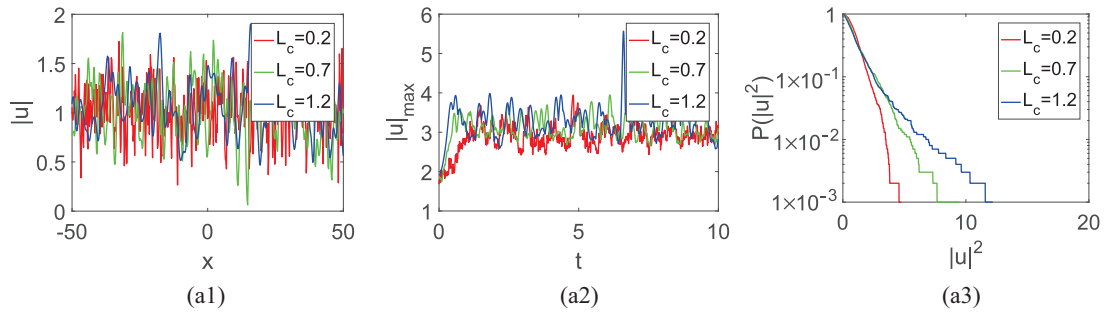


FIG. 6. Numerical results of initial conditions with fixed value of $\mu = 0.4$ and three different values of $L_c = 0.2$ (the red line), $L_c = 0.7$ (the green line), and $L_c = 1.2$ (the blue line). (a1) Initial field intensity of $u(0, x)$. (a2) Evolution of the maximum field amplitude versus t . (a3) Probability density function for the field intensity after 100 units along the t axis.

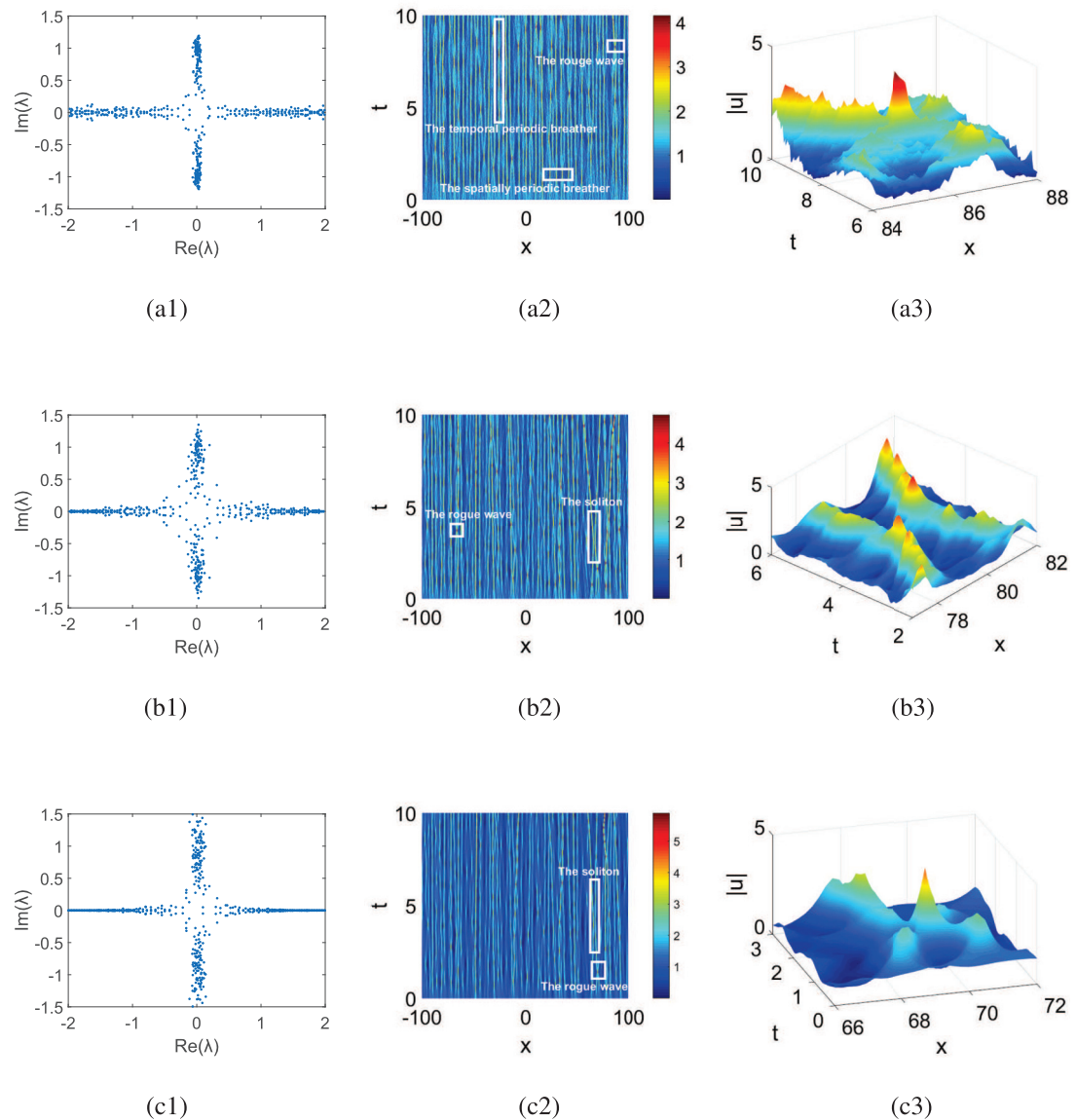


FIG. 7. Numerical results of initial conditions with fixed value of $\mu = 0.4$ and three values of $L_c = 0.2$, $L_c = 0.7$, $L_c = 1.2$. [(a1)–(c1)] Spectra portraits; [(a2)–(c2)] Space-time diagram of chaotic wave fields; [(a3)–(c3)] The three-dimensional view of the large amplitude structures extracted from [(a2)–(c2)].

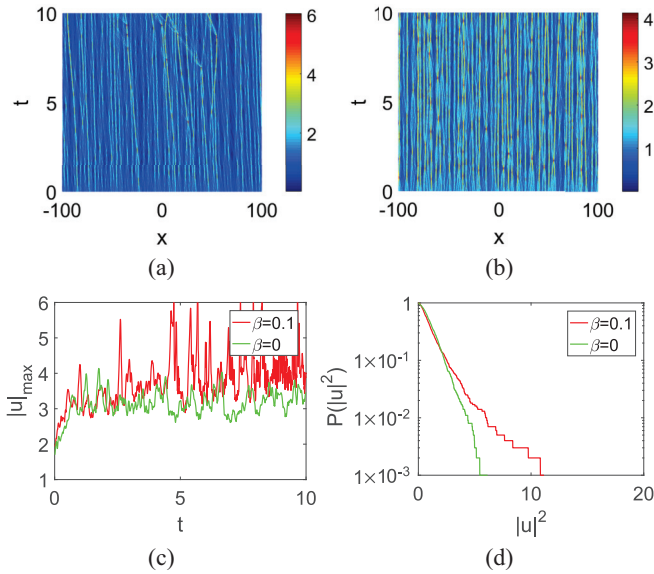


FIG. 8. Numerical results of the KE equation [$\beta = 0.1$ in Eq. (1)] and NLS equation [$\beta = 0$ in Eq. (1)] under the same initial conditions with the random parameters $\mu = 0.4$ and $L_c = 0.5$. (a) Chaotic wave field of the KE equation. (b) Chaotic wave field of NLS equation. (c) Evolution of the maximum field amplitude versus t . (d) Probability density function of the field intensity after 100 units along the t axis.

higher-order nonlinear coefficient β on the chaotic wave fields through some numerical results. We choose the same initial condition with the random parameters $\mu = 0.4$ and $L_c = 0.5$ to stimulate the chaotic wave fields for Eq. (1) with $\beta = 0.1$ and $\beta = 0$, respectively. Through the comparison of numerical results, we find that due to the high-order nonlinear effects of Eq. (1), the peak amplitude of the chaotic wave field evolved by Eq. (1) is around six in Fig. 8(a), which is higher than the peak amplitude of the NLS equation, which is around four in Fig. 8(b). It can also be observed that the maximum field amplitude of Eq. (1) is greater than that of the NLS equation in Fig. 8(c). From Fig. 8(d), we can see that the PDF curve of the field intensity of Eq. (1) is higher than that of the NLS equation, indicating that under the same initial condition, the probability of generating a rogue wave in Eq. (1) is higher than that in the NLS equation. The above results demonstrate that the existence of higher-order nonlinear effects could lead to large-amplitude chaotic wave field, which is more easier to generate the rogue wave.

IV. SUMMARY AND DISCUSSION

In this article, we investigated the integrable turbulence and characteristics of chaotic wave field in the KE equation. First of all, to give the correspondence between the spectrum and different solutions, we computed numerically the spectral portraits of soliton, breather, and rogue wave solutions via the Fourier collocation method, as seen in Fig. 2. Then we performed the numerical simulations on Eq. (1) under the initial condition of a plane wave with random noise to stimulate the chaotic wave fields. As seen from Fig. 3(a)–3(b) about the variations of initial field intensity and maximum field amplitude with the standard deviation μ , it's found that large standard deviation leads to the strong chaotic deviation around the continuous wave, fast convergence speed to the chaotic state, and high peak amplitude of the wave field. By comparing the PDF of the field intensity obtained after propagating 100 units of distance with different values of μ in Fig. 3(c), we found that the PDF tail gets higher as μ increases which indicates the generation probability of a rogue wave will significantly improve. Through discussing the spectral portraits, corresponding integrable turbulence and proportion of solution contents in the chaotic wave field, we got the the transition phenomenon from breather turbulence to soliton turbulence, and proved the generation of rogue wave (see Figs. 4 and 5). Furthermore, we studied the influence of correlation length L_c on the evolution of initial plane wave with random noise and obtain the similar effects to the parameter μ , except that the types of solution contents are not related to L_c (see Figs. 6 and 7). To demonstrate the differences of chaotic wave fields in the KE system and NLS equation, we analyzed the higher-order nonlinear effects in the KE equation, which led to a larger amplitude of the chaotic wave field and a higher probability of generating rogue waves. These studies will help to understand the integrable turbulence and generation of rogue waves in the KE equation from the numerical and statistical viewpoint.

The data that support the findings of this study are available from the corresponding author upon reasonable request.

ACKNOWLEDGMENTS

This work was partially supported by the Beijing Natural Science Foundation (Grants No. 1232022 and No. 1212007).

- [1] N. Akhmediev, J. M. Soto-Crespo, and N. Devine, Breather turbulence versus soliton turbulence: Rogue waves, probability density functions, and spectral features, *Phys. Rev. E* **94**, 022212 (2016).
- [2] F. Fedele, Rogue waves in oceanic turbulence, *Physica D* **237**, 2127 (2008).
- [3] K. Dysthe, H. E. Krogstad, and P. Müller, Oceanic rogue waves, *Annu. Rev. Fluid Mech.* **40**, 287 (2008).
- [4] D. R. Solli, C. Ropers, P. Koonath, and B. Jalali, Optical rogue waves, *Nature (London)* **450**, 1054 (2007).
- [5] M. Onorato, S. Residori, U. Bortolozzo, A. Montina, and F. T. Arecchi, Rogue waves and their generating mechanisms in different physical contexts, *Phys. Rep.* **528**, 47 (2013).
- [6] N. Akhmediev, J. M. Soto-Crespo, and A. Ankiewicz, Extreme waves that appear from nowhere: On the nature of rogue waves, *Phys. Lett. A* **373**, 2137 (2009).
- [7] Y. L. Ma and B. Q. Li, Analytic rogue wave solutions for a generalized fourth-order Boussinesq equation in fluid mechanics, *Math. Methods Appl. Sci.* **42**, 39 (2019).

- [8] B. Q. Li and Y. L. Ma, N-order rogue waves and their novel colliding dynamics for a transient stimulated Raman scattering system arising from nonlinear optics, *Nonlinear Dyn.* **101**, 2449 (2020).
- [9] M. Wang, B. Tian, Y. Sun, H. M. Yin, and Z. Zhang, Mixed lump-stripe, bright rogue wave-stripe, dark rogue wave-stripe and dark rogue wave solutions of a generalized Kadomtsev-Petviashvili equation in fluid mechanics, *Chin. J. Phys.* **60**, 440 (2019).
- [10] C. N. Kumar, R. Gupta, A. Goyal, S. Loomba, T. S. Raju, and P. K. Panigrahi, Controlled giant rogue waves in nonlinear fiber optics, *Phys. Rev. A* **86**, 025802 (2012).
- [11] S. Wabnitz, C. Finot, J. Fatome, and G. Millot, Shallow water rogue wavetrains in nonlinear optical fibers, *Phys. Lett. A* **377**, 932 (2013).
- [12] A. H. Salas, S. A. El-Tantawy, and J. E. Castillo, The hybrid finite difference and moving boundary methods for solving a linear damped nonlinear Schrödinger equation to model rogue waves and breathers in plasma physics, *Math. Probl. Eng.* **2020**, 6874870 (2020).
- [13] M. Onorato, A. R. Osborne, and M. Serio, Modulational instability in crossing sea states: A possible mechanism for the formation of freak waves, *Phys. Rev. Lett.* **96**, 014503 (2006).
- [14] G. Biondini and E. Fagerstrom, The integrable nature of modulational instability, *SIAM J. Appl. Math.* **75**, 136 (2015).
- [15] J. M. Dudley, F. Dias, M. Erkintalo, and G. Genty, Instabilities, breathers and rogue waves in optics, *Nat. Photonics* **8**, 755 (2014).
- [16] J. M. Soto-Crespo, N. Devine, and N. Akhmediev, Integrable turbulence and rogue waves: Breathers or solitons? *Phys. Rev. Lett.* **116**, 103901 (2016).
- [17] X. Y. Xie, S. K. Yang, C. H. Ai, and L. C. Kong, Integrable turbulence for a coupled nonlinear Schrödinger system, *Phys. Lett. A* **384**, 126119 (2020).
- [18] L. Wang, Z. Y. Yan, and B. L. Guo, Numerical analysis of the Hirota equation: Modulational instability, breathers, rogue waves, and interactions, *Chaos* **30**, 013114 (2020).
- [19] G. Michel, F. Bonney, G. Ducroz, G. Prabhudesai, A. Cazaubiel, F. Copie, A. Tikan, P. Suret, S. Randoux, and E. Falcon, Emergence of peregrine solitons in integrable turbulence of deep water gravity waves, *Phys. Rev. Fluids* **5**, 082801(R) (2020).
- [20] Y. N. Tang, Z. J. Liang, and W. X. Xie, The local wave phenomenon in the quintic nonlinear Schrödinger equation by numerical methods, *Nonlinear Dyn.* **108**, 1547 (2022).
- [21] P. A. Clarkson and J. A. Tuszynski, Exact solutions of the multidimensional derivative nonlinear Schrödinger equation for many-body systems of criticality, *J. Phys. A: Math. Gen.* **23**, 4269 (1990).
- [22] R. S. Johnson, On the modulation of water waves in the neighbourhood of $kh \approx 1.363$, *Proc. R. Soc. London Ser. A* **357**, 131 (1977).
- [23] E. Parasuraman, Modulational instability criterion for optical wave propagation in birefringent fiber of Kundu-Eckhaus equation, *Optik-Int. J. Light Electron. Opt.* **243**, 167429 (2021).
- [24] S. Kakei, N. Sasa, and J. Satsuma, Bilinearization of a generalized derivative nonlinear Schrödinger equation, *J. Phys. Soc. Jpn.* **64**, 1519 (1995).
- [25] G. Z. Tu, On Liouville integrability of zero-curvature equations and the Yang hierarchy, *J. Phys. A: Math. Gen.* **22**, 2375 (1989).
- [26] X. G. Geng, A hierarchy of non-linear evolution equations its Hamiltonian structure and classical integrable system, *Physica A* **180**, 241 (1992).
- [27] A. Kundu, Landau-Lifshitz and higher-order nonlinear systems gauge generated from nonlinear Schrödinger-type equations, *J. Math. Phys.* **25**, 3433 (1984).
- [28] P. A. Clarkson, C. M. Cosgrove, Painlevé analysis of the nonlinear Schrödinger family of equations, *J. Phys. A: Math. Gen.* **20**, 2003 (1987).
- [29] Q. L. Zha, On nth-order rogue wave solution to the generalized nonlinear Schrödinger equation, *Phys. Lett. A* **377**, 855 (2013).
- [30] D. Q. Qiu, J. S. He, Y. S. Zhang, K. Porsezian, The Darboux transformation of the Kundu-Eckhaus equation, *Proc. R. Soc. A* **471**, 20150236 (2015).
- [31] D. Q. Qiu and W. G. Cheng, The nth-order degenerate breather solution for the Kundu-Eckhaus equation, *Appl. Math. Lett.* **98**, 13 (2019).
- [32] P. Wang, B. Tian, K. Sun, and F. H. Qi, Bright and dark soliton solutions and Bäcklund transformation for the Eckhaus-Kundu equation with the cubic-quintic nonlinearity, *Appl. Math. Comput.* **251**, 233 (2015).
- [33] X. Geng and H. W. Tam, Darboux transformation and soliton solutions for generalized nonlinear Schrödinger equations, *J. Phys. Soc. Jpn.* **68**, 1508 (1999).
- [34] L. L. Wen and E. G. Fan, The Riemann-Hilbert approach to focusing Kundu-Eckhaus equation with nonzero boundary conditions, *Mod. Phys. Lett. B* **34**, 2050332 (2020).
- [35] K. Khusnutdinova, Nonlinear waves in integrable and non-integrable systems (mathematical modeling and computation 16) by Jianke Yang, *Bull. London Math. Soc.* **47**, 188 (2015).
- [36] G. M. Muslu and H. A. Erbay, Higher-order split-step Fourier schemes for the generalized nonlinear Schrödinger equation, *Math. Comput. Simul.* **67**, 581 (2005).
- [37] B. F. Sanders, N. D. Katopodes, and J. P. Boyd, Spectral modeling of nonlinear dispersive waves, *J. Hydraulic Eng.* **124**, 2 (1998).
- [38] N. Akhmediev, A. Ankiewicz, and J. M. Soto-Crespo, Rogue waves and rational solutions of the nonlinear Schrödinger equation, *Phys. Rev. E* **80**, 026601 (2009).
- [39] D. S. Agafontsev and V. E. Zakharov, Integrable turbulence and formation of rogue waves, *Nonlinearity* **28**, 2791 (2015).